Nano Research

Open Access

Research Article

Controllable synthesis of biomimetic wood stem nanoporous high entropy oxides catalysts for oxygen evolution reaction

Wei Wang[1], Weiqi Wang[1], Huihui Wang[2], Xing Lu[1] ✉, Jinwen Zhang[3] ✉, and Yunzhuo Lu[1] ✉

[1] *School of Materials Science and Engineering, Dalian Jiaotong University, Dalian 116028, China*
[2] *School of Intelligence and Electronic Engineering, Dalian Neusoft University of Information, Dalian 116023, China*
[3] *Guangdong Key Laboratory of Materials and Equipment in Harsh Marine Environment, Guangzhou Maritime University, Guangzhou 510725, China*

Cite this article: *Nano Research*, **2025**, *18*, 94907002. https://doi.org/10.26599/NR.2025.94907002

ABSTRACT: Bubbles generated during the oxygen evolution reaction (OER) in water splitting readily adhere to the electrode surface, thereby impeding contact between the electrolyte and the active sites, thereby increasing the overpotential. Consequently, it is imperative to elucidate the bubble release behavior and engineer electrodes that facilitate faster bubble release. In this study, inspired by the wood stem of the Norway spruce, we synthesized a gradient nanoporous high-entropy oxide (GNP-HEO) electrode with a controllable pore size. The GNP-HEO, featuring a well-controlled gradient in pore size, is achieved through a straightforward strategy combining selective laser melting with selective phase dissolution. This unique gradient nanoporous structure not only facilitates bubble release but also diminishes the bubble shielding effect in OER, thereby enhancing electrocatalytic performance. The affect interaction of Al, Co, Cr, Fe, and Ni, coupled with the gradient nanoporous structure, yields exceptional OER performance, evidenced by an overpotential of 250 mV at a current density of 50 mA/cm^2 and a Tafel slope of 38.0 mV/dec in 1 M KOH. Density functional theory calculations confirm that the GNP-HEO adheres to the adsorbate evolution mechanism reaction pathway and exhibits significant stability. This work highlights a promising approach for the design and synthesis of high-performance OER electrocatalysts.

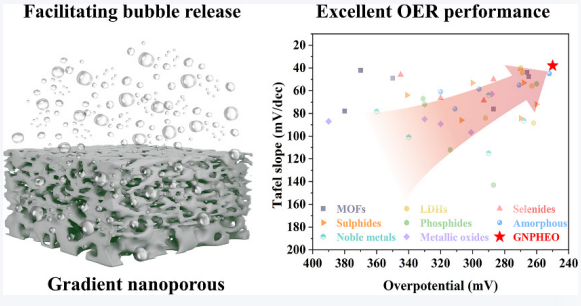

KEYWORDS: oxygen evolution reaction, high-entropy oxides, selective phase dis-solution, selective laser melting, gradient nanoporous

1 Introduction

Hydrogen is recognized as a clean, safe energy source pivotal for reducing carbon emissions. The development of cost-effective, environmentally friendly water-splitting technology is a critical area of research for sustainable hydrogen production [1–3]. This process involves two key reactions: the hydrogen evolution reaction (HER) at the cathode and the oxygen evolution reaction (OER) at the anode [4, 5]. The OER is complex, requiring the transfer of four protons and electrons, which results in high energy consumption [6]. Consequently, the exploration of highly active electrocatalysts that can lower the energy barrier and enhance reaction rates is essential.

Received: July 15, 2024; **Revised:** August 10, 2024
Accepted: August 23, 2024

✉Address correspondence to Xing Lu, lu@djtu.edu.cn; Jinwen Zhang, zjw@gzmtu.edu.cn; Yunzhuo Lu, luyz@djtu.edu.cn

In recent years, nanoporous high entropy alloy (HEA) electrocatalysts have emerged as a significant focus in water-splitting research, attributed to their distinctive benefits: high entropy effects, lattice distortion, sluggish diffusion, and cocktail effects [7–9]. These effects collectively enhance the catalytic activity: High entropy and lattice distortion increase the number of active sites for catalytic reactions, while sluggish diffusion contributes to catalyst stability. The cocktail effect further boosts catalytic efficiency [10, 11]. However, the nanoporous structure is not conducive to mass transferring and limits the reaction kinetics [12]. Additionally, the mesoporous structure may impede gas release, potentially damaging the nanoporous framework. Therefore, developing highly efficient, cost-effective, and stable catalysts remains a critical challenge.

The total overpotential of an OER is determined by three factors: activation overpotential (η_{act}), ohmic overpotential (η_{ohm}), and concentration overpotential (η_{con}) [13, 14]. To date, enhancements in OER catalysts have predominantly focused on modifying

chemical properties to reduce η_{act}, often neglecting the impacts of η_{ohm} and η_{con}. However, these latter two factors significantly influence bubble behavior during water splitting [15]. Bubbles that form and adhere to the catalyst surface during OER can disrupt the contact between the active sites and the electrolyte, thereby diminishing the process efficiency [16]. Therefore, understanding bubble release during electrolysis and developing electrocatalysts that promote the rapid escape of bubbles are essential for improving water splitting efficiency.

Nature serves as an invaluable mentor for addressing scientific challenges. The wood stem of the spruce in Norway exhibits a naturally occurring porosity gradient, characterized by the large pores of earlywood and the smaller pores of latewood (Fig. 1(a)). This gradient porous structure not only facilitates water transport and enhances mechanical stability but may also improve the efficiency of water-splitting processes by accelerating bubble release [17]. By bionic this structure, developing gradient nanoporous electrodes could potentially enhance OER performance. However, traditional fabrication methods struggle to produce such controllable gradient structures in electrodes.

Over the past decades, selective laser melting (SLM) has become increasingly popular due to its precise control over shape, high production rate, and efficiency. Unlike other methods, SLM allows for meticulous control over the solidification microstructure and composition at specific locations, laying a solid theoretical foundation for fabricating gradient nanoporous structured electrodes [18, 19]. In this report, we introduce a novel approach that combines SLM with selective phase dissolution (SPD) to create AlCoCrFeNi high entropy oxides with a gradient nanoporous structure, featuring pore sizes ranging from 7 to 32 nm. The resulting AlCoCrFeNi oxides electrode demonstrates superior performance in alkaline solution OER electrocatalysis. Specifically, it achieves an overpotential of only 250 mV at 50 mA/cm^2 and a low Tafel slope of 38 mV/dec in 1 M KOH, outperforming most reported OER electrocatalysts.

2 Experimental section

2.1 Materials synthesis

The raw material used was spherical AlCoCrFeNi high entropy alloy powder, sourced from Beijing Yanbang New Materials Technology Co., Ltd. The particle size and morphology were detailed in Fig. S1 in the Electronic Supplementary Material (ESM). Observations indicate that the powder is highly spherical, lacks any planar defects, and displays a uniform particle size distribution. The size range of the powder particles was 15–53 μm, with an average particle size of 28.3 μm. The elemental composition of the powder was determined using energy-dispersive spectroscopy (EDS) via a scanning electron microscopy (SEM).

SLM samples using the FF-M180D (FastForm, China) machine, which was equipped with a 500 W fiber laser and a beam spot diameter of 125 μm, were prepared. In the SLM process, the powder layer thickness was set to 30 μm, the scanning spacing was set to 100 μm, and the scanning direction between consecutive layers (N+1 and N) was adjusted to 67°. To minimize residual stress, the substrate was preheated to 100 °C before printing. The SLM process must also be conducted in an argon atmosphere to prevent oxidation. After printing, the sample was separated from the substrate using a wire-cutting device, then sequentially polished with 240–4000 grit sandpaper until no scratches remain. The polished sample was cleaned ultrasonically and dried in a vacuum oven. For the preparation of nanoporous high-entropy oxide (HEO) electrodes, electrochemical SPD was employed. The printed HEA was used as the working electrode, a Pt plate was used as the counter electrode, and an Ag/AgCl electrode was used as the reference. All samples undergone SPD in a 0.01 M H_2SO_4 aqueous solution for 48 h, controlled by a two-step potentiostatic method.

2.2 Characterization

An X-ray diffractometer (XRD) was employed to analyze the phase composition of both printed and selectively dissolved samples. The microstructure was characterized using a Zeiss Ultra 55 SEM and a

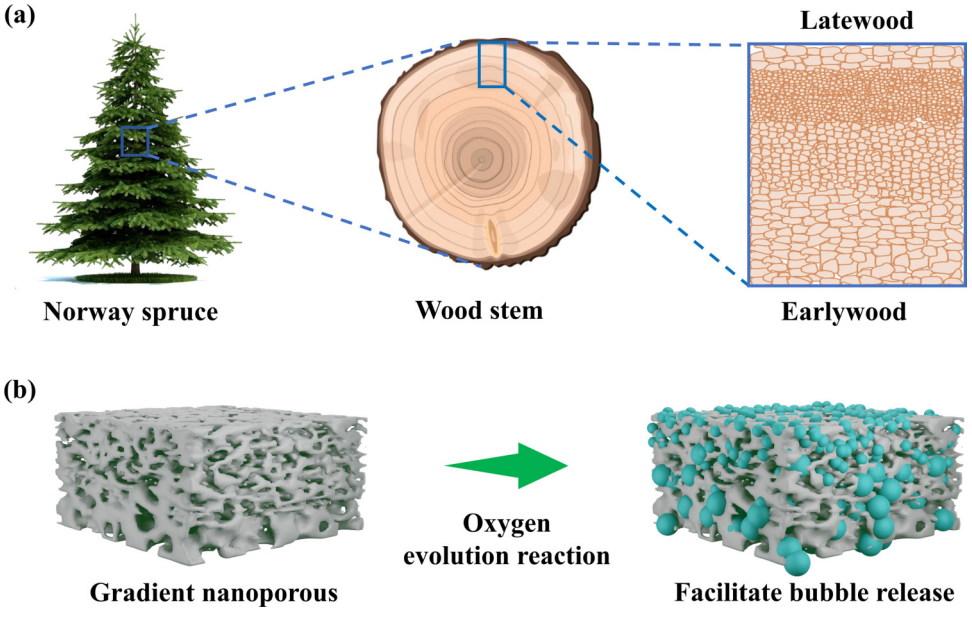

Figure 1 Biomimetic wood stem for the synthesis of gradient nanoporous high entropy oxides electrocatalysts. (a) Schematic of the wood stem with gradient porous. (b) Schematic illustration showing the GNP-HEO electrode and the OER on the GNP-HEO electrode.

JSM 2100F transmission electron microscopy (TEM). These instruments were equipped with an energy spectrometer to determine the chemical composition of the samples. Additionally, X-ray photoelectron spectroscopy (XPS) analyses were conducted using a Thermo Scientific ESCALAB 250 XI (Thermo Fisher Scientific, USA) to examine the chemical binding states.

2.3 Electrochemical measurements

To further evaluate the electrochemical performance of the electrodes, measurements were conducted using a CHI760E electrochemical workstation within a standard three-electrode system. The printed and selectively dissolved AlCoCrFeNi high entropy alloys served as the working electrodes, with a Pt sheet as the counter electrode, and Ag/AgCl as the reference electrode. To ensure accurate and stable polarization curves, 200 cycles of cyclic voltammetry (CV) were performed before testing, setting a potential window from 0.05 to 1.0 V versus reversible hydrogen electrode (RHE) at a scan rate of 50 mV/s. Once a stable current was achieved, the polarization curve was recorded using linear sweep voltammetry (LSV) at a scan rate of 5 mV/s. Potentials were adjusted against the RHE according to the Nernst equation: $E_{(RHE)} = E(Ag/AgCl) + 0.0591pH + 0.198$ V. Electrochemical impedance spectroscopy (EIS) was performed at frequencies ranging from 0.01 Hz to 100 kHz with a sinusoidal alternating current (AC) signal amplitude of 5 mV. Solution resistance (R_s) was determined via EIS for iR correction. Electrode durability was assessed through chronopotentiometry and 2000 cycles of cyclic voltammetry.

2.4 Density function theory (DFT) calculations

The DFT was implemented in the Vienna *ab initio* simulation package (VASP) in all calculations. The exchange-correlation potential was described by using the generalized gradient approximation of Perdew–Burke–Ernzerhof (GGA-PBE). The projector augmented-wave (PAW) method was employed to treat interactions between ion cores and valence electrons. The plane-wave cutoff energy was fixed to 450 eV. Given structural models were relaxed until the Hellmann–Feynman forces were smaller than –0.02 eV/Å and the change in energy smaller than 10^{-5} eV was attained. Grimme's DFT-D3 methodology was used to describe the dispersion interactions among all the atoms in adsorption models.

3 Results

3.1 The preparation and characterization of tunable three-dimensional (3D) microstructure

Figure 1 illustrates that the schematic of the biomimetic wood stems GNP-HEO electrode. The preparation process consists of two primary steps: printing the precursor AlCoCrFeNi alloy using SLM and creating nanoporous high entropy oxides through SPD. To explore the impact of SLM processing parameters on microstructure, a variety of samples are prepared using different laser powers (P) and scanning speeds (v), as detailed in Table S1 in the ESM. The XRD patterns of the printed alloys, displayed in Fig. S2 in the ESM, reveal two distinct phases, indicating that SLM parameters do not alter the phase compositions of the AlCoCrFeNi high entropy alloys.

SEM images of post-SPD, varying with printing parameters, are shown in Fig. S3 in the ESM. TEM analysis confirms the presence of nanopores and the effect of SLM parameters on pore size (Fig. S4 in the ESM). Scanning TEM (STEM) images and corresponding EDS elemental mappings of the nanoporous AlCoCrFeNi oxides, shown in Fig. S5 in the ESM, demonstrate the uniform distribution of Al, Co, Cr, Fe, Ni, and O elements. Figure S6 in the ESM shows the HRTEM image of nanoporous high-entropy AlCoCrFeNi oxides, indicating an interlayer distance close to 0.203 nm, corresponding well with the d-spacing of the (110) planes of the Fe-Cr-rich phase. The slightly smaller interlayer distance than the standard can be attributed to lattice distortion effects. The formation of these nanoporous structures is attributed to spinodal decomposition during the printing process, where highly interconnected Fe-Cr rich and Ni-Al rich phases form due to differences in mixing enthalpy between atom pairs. The Ni-Al rich phases, being more soluble in 0.01 M H_2SO_4, dissolve more readily than the Fe-Cr rich phases, creating highly connected pores. XRD characterization confirms that the precursor alloy comprises these phases (Fig. S2 in the ESM). After SPD, the characteristic peak of the Ni-Al rich phases disappears, indicating the completion of the reaction (Fig. S7 in the ESM). Notably, increased laser power and decreased scan speed result in larger pore sizes, as shown in Table S1 in the ESM.

3.2 Designing and preparing GNP-HEO

The method for regulating the nanoporous structure can be readily achieved by altering the microstructure of the precursor alloy rather than modifying its composition. This adjustment is straightforward by varying the cooling rate. The controllable manufacturing of gradient nanoporous high entropy oxides (GNP-HEO) is underpinned by a physical understanding of the systematic correlation between SLM process parameters, cooling rates, and resultant microstructures. Typically, laser energy density is influenced by several variables including laser power, scanning speed, beam diameter, scanning spacing (hatch distance), and layer thickness. In this study, we employ the P/v ratio (linear energy density) to gauge laser energy input while keeping other processing variables constant. Figure 2(a) illustrates the relationship between nanoporous oxide pore size and linear energy density, which follows a linear equation: $F = -0.12 + 25.52 \times (P/v)$. Using this quantitative relationship, we selected four distinct combinations of P and v (220 W/1200 mm/s, 420 W/800 mm/s, 320 W/400 mm/s, 420 W/400 mm/s) to fabricate a gradient in the high entropy alloy precursor from top to bottom. After SPD, GNP-HEO with pore sizes ranging from 7 to 32 nm from top to bottom are successfully synthesized, as depicted in Fig. 2(b). The chemical composition of the GNP-HEO is presented in Table S2 in the ESM. These results demonstrate that GNP-HEO with a spatial gradient can be effectively synthesized using a straightforward strategy that combines SLM and SPD.

3.3 Electrocatalytic activity and stability for OER

To assess the electrochemical performance of the nanoporous high-entropy oxides electrode, all tests are conducted in a 1 M KOH solution using a three-electrode system. Continuous cyclic voltammetry scanning precedes OER testing to stabilize the electrode. The electric potential is normalized to a RHE using the equation: $E_{(RHE)} = E(Ag/AgCl) + 0.0591pH + 0.198$ V. The LSV curves, as shown in Fig. 3(a), reveal that the nanoporous catalyst exhibits a lower overpotential at identical current densities compared to bulk high-entropy alloys. This improvement is likely due to the increased surface area of the nanoporous structure,

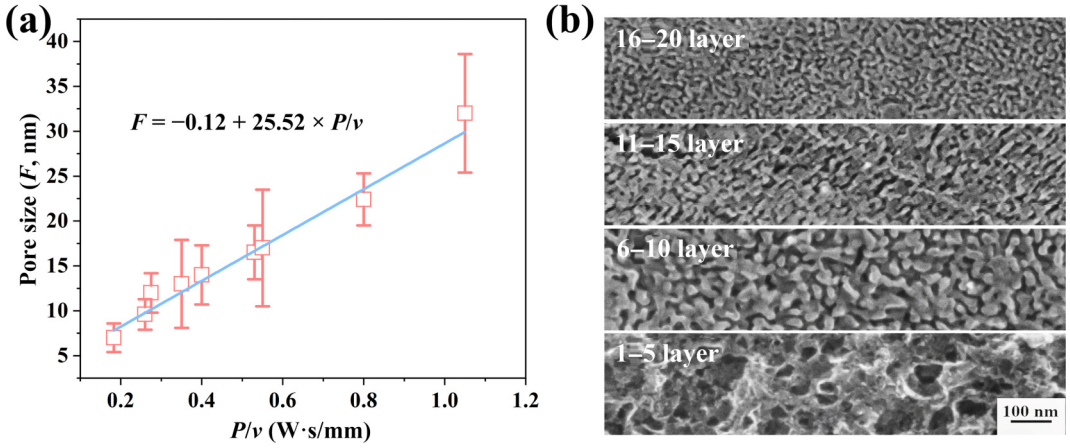

Figure 2 Variation of pore size with line energy density and designing of GNP-HEO. (a) Pore sizes, *F* of the nanoporous high entropy oxides, as a function of linear energy density *P*/*v*. (b) 4-layered GNP-HEO by SLM with a thickness of ~ 0.03 mm for each layer.

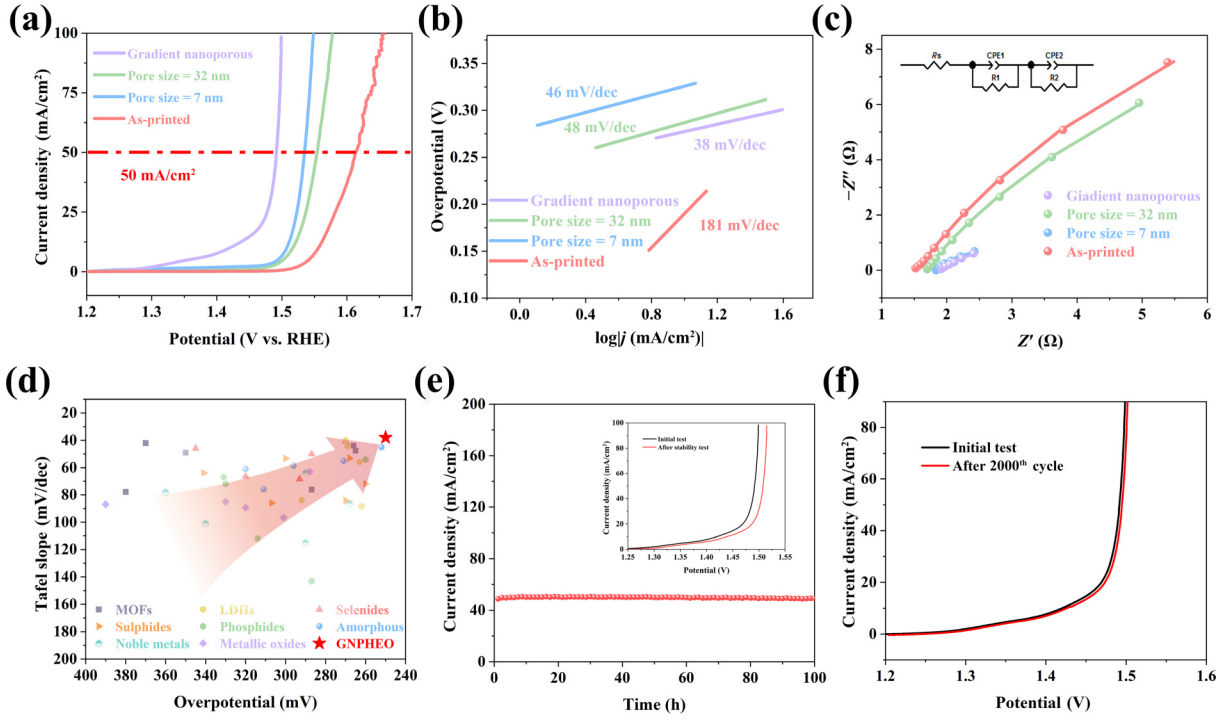

Figure 3 Electrochemical characterizations of the GNP-HEO for OER in 1.0 M KOH. (a) Polarization curves. (b) Tafel plots. (c) Nyquist plots measured at open circuit potential. (d) The comparison in overpotential (50 mA/cm^2) and Tafel slope of our work with other reported catalysts. (e) The long-term durability curves. (f) LSV curves of the initial and after 2000th cycle LSV curves.

which provides more active sites for OER. Notably, the gradient nanoporous electrode achieves an overpotential of only 250 mV at a current density of 50 mA/cm^2, demonstrating optimal electrocatalytic performance. It is lower than the values for nanoporous electrodes with pore sizes of 7 nm (≈ 300 mV) and 32 nm (≈ 320 mV), as well as the bulk HEA (≈ 380 mV). The Tafel slope, a crucial parameter for assessing catalyst performance and the reaction mechanism in OER, is derived from the polarization curves. As depicted in Fig. 3(b), the GNP-HEO shows superior kinetics with the lowest Tafel slope of 38 mV/dec, significantly lower than the 181 mV/dec observed for the as-printed alloy. This indicates faster catalytic kinetics due to O_2 formation being the dominant intermediate reaction at the catalytic sites, with electron–proton reaction steps being rate-determining for OER [20]. GNP-HEO presents a smaller Tafel slope of 38 mV/dec compared to 181 mV/dec for as-printed alloy, indicating faster catalytic kinetics for GNP-HEO. In addition, chemical reactions with O_2 formation as an intermediate on the catalytic sites are dominant for GNP-HEO, and the impact of the electron–proton reaction steps is the primary step for the OER [21]. Electrochemical impedance spectroscopy further elucidates the interface reactions and electrode kinetics. The Nyquist plots in Fig. 3(c) display minimal semicircular radius for GNP-HEO among all tested electrocatalysts, underscoring its exceptional performance. These observations demonstrate the important role of the electrode structure in the alkaline OER electrocatalysis. Figure 3(d) and Table S3 in the ESM compare the overpotential and Tafel slope of GNP-HEO at 50 mA/cm^2 against recent state-of-the-art OER electrocatalysts, demonstrating its superior activity for alkaline OER [22–62].

Reliable electrode stability is crucial and can be assessed through chronopotentiometry. Figure 3(e) illustrates the electrochemical stability of the GNP-HEO electrode, maintained at 50 mA/cm^2 for 100 h in 1 M KOH electrolyte. The inset of Fig. 3(e) compares the initial and post-stability test OER polarization curves. It shows that the overpotential increased by only 20 mV, indicating minimal change in activity. Moreover, the LSV curve of GNP-HEO, shown in Fig. 3(f), remains consistent with the first cycle after 2000 cycles, further confirming the electrode's excellent long-term stability. This remarkable cyclic stability is attributed to the stable gradient nanoporous structure, which facilitates efficient ion transport and electron conduction [63]. Figure S8 in the ESM displays the TEM image of nanoporous high-entropy AlCoCrFeNi oxides after the long-term stability test, showing that it retains almost the same structure as the initial one.

3.4 Visualization of bubble release behaviors

To elucidate the reasons behind the superior electrochemical performance of GNP-HEO and its structural impact on bubble dynamics, the behavior of bubbles on the electrode surface is observed using a high-speed camera. Figure 4 depicts bubble release at 50 mA/cm^2 across three different electrode structures. As demonstrated in Figs. 4(a)–4(f), electrodes with a uniform small pore structure or a gradient nanoporous structure release smaller bubbles compared to those with uniform large pores. Notably, the electrode with a gradient nanoporous structure shows the quickest bubble release time at only 4.6 s, while the electrode with uniform large pores exhibits the slowest, taking 338.64 s for bubbles to detach as shown in Figs. 4(g)–4(i). The smaller average bubble diameter and faster release enhance the exposure of active sites, decrease reactant transfer resistance, and reduce ohmic drop within the electrode, all of which contribute to improved catalytic activity. The following section will delve into how the gradient nanoporous structure specifically accelerates the bubble release mechanism.

3.5 The multicomponent synergetic effect of HEA

XPS was carried out to further investigate the surface chemical composition and valence states of the GNP-HEO before and after OER, the results are shown in Fig. 5. To ensure the accuracy of the experimental results, the binding energy of all elements is calibrated by the C 1s peak at 284.8 eV. According to the XPS spectra of GNP-HEO, Al, Co, Cr, Fe, Ni, and O elements exist on the surface. In the Al 2p spectra, the Al 2p peaks with binding energies at 75.1 eV belong to the aluminum oxides. After OER, the peaks located at 73.4 and 76.7 eV are ascribed to Al^{3+} $2p_{3/2}$ and Al^{3+} $2p_{1/2}$, respectively [64]. The surface of the GNP-HEO electrode contains Al_2O_3 both before and after OER. Figure 5(b) displays that the Co 2p spectra could be resolved into three distinctive peaks. The peaks located at 778.5 eV (Co^0 $2p_{3/2}$) and 793.3 eV (Co^0 $2p_{1/2}$) are characteristic of metallic Co [65]. The peaks located at 782.4eV (Co^{2+} $2p_{3/2}$) should be ascribed to the Co–O bond, which may be caused by natural oxidation. After OER, the characteristic peaks of metallic Co (778.5 eV) could still be observed and low valence states (Co^0, Co^{2+}) could be oxidized to a higher valence (Co^{3+}). As shown in Fig. 5(c), Cr 2p spectra peaks could be deconvoluted into four peaks before OER. The XPS peaks at 574.2, 576.8, 583.4, and 586.6 eV on the surface of GNP-HEO electrode before OER can be attributed to Cr^0 $2p_{3/2}$, Cr^{3+} $2p_{3/2}$, Cr^0 $2p_{1/2}$, and Cr^{3+} $2p_{1/2}$. After OER, the signal from Cr 2p is too weak to be detected due to the dissolution during the OER process [66]. For the Fe 2p spectrum in Fig. 5(d), the peaks at 706.5 and 711.25 eV are assigned to Fe and Fe_2O_3. After OER, two main peaks are observed, the peak at 709.4 eV is assigned to the metallic iron; and the peak at 712.3 eV is assigned to FeOOH, which demonstrates the presence of +3 valence states of Fe [67]. As shown in the spectrum of Ni 2p in Fig. 5(e), the peaks at 852.9,

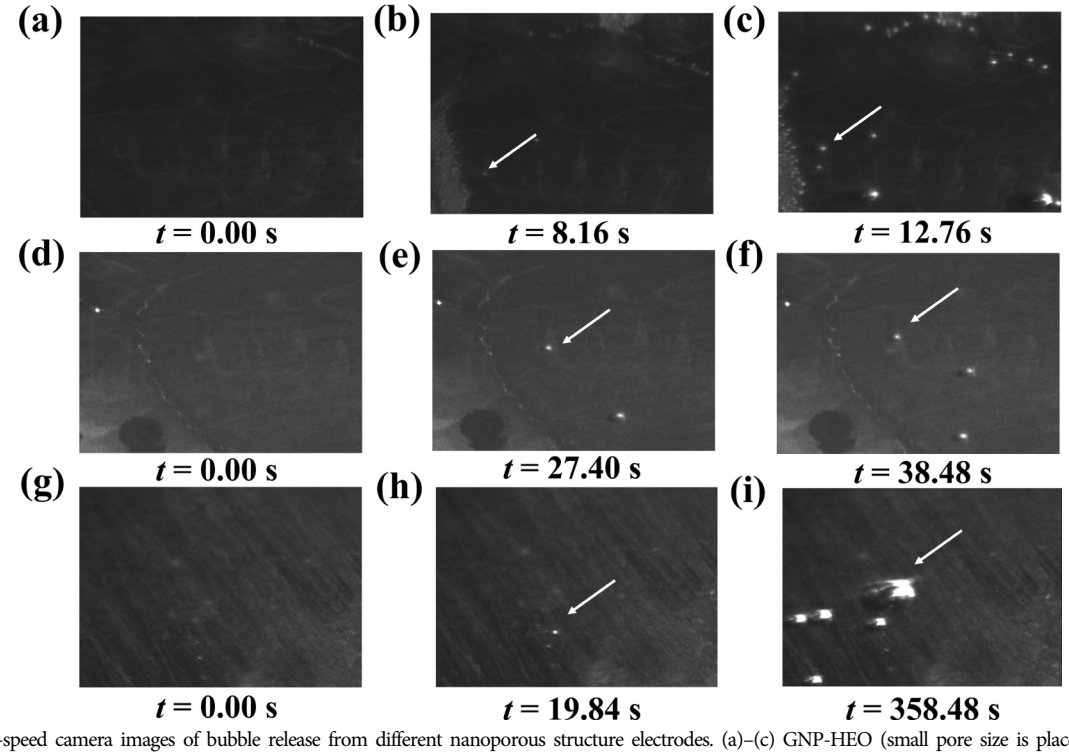

Figure 4 High-speed camera images of bubble release from different nanoporous structure electrodes. (a)–(c) GNP-HEO (small pore size is placed facing counter electrode in the gradient structure), (d)–(f) uniform small pores (pore size = 7 nm), and (g)–(i) uniform large pores (pore size = 32 nm).

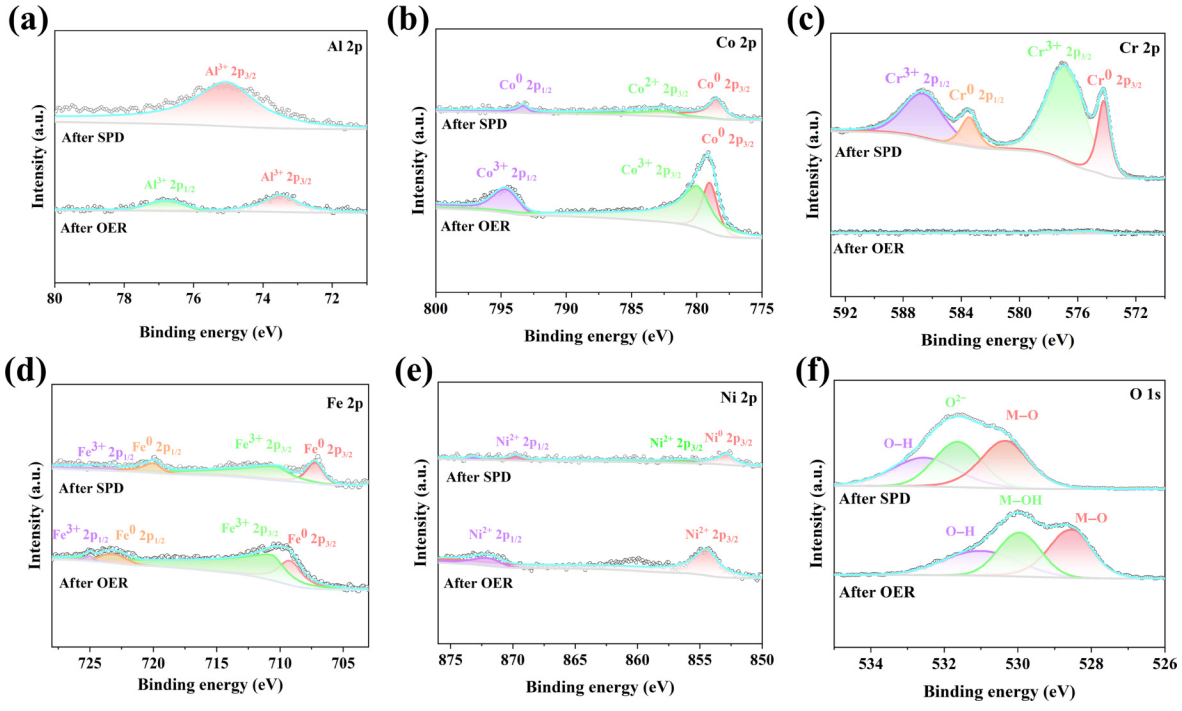

Figure 5 XPS high-resolution spectra of (a) Al 2p, (b) Co 2p, (c) Cr 2p, (d) Fe 2p, (e) Ni 2p, and (f) O 1s for the gradient nanoporous AlCoCrFeNi HEO before and after OER test.

856.1, and 869.7 eV are assigned to Ni^0 $2p_{3/2}$, Ni^{2+} $2p_{3/2}$, and Ni^0 $2p_{1/2}$, respectively. After OER, the peaks located at 854.5eV (Ni^{2+} $2p_{3/2}$) and 872.0 eV (Ni^{2+} $2p_{1/2}$) should be ascribed to the Ni–O bond [66]. For the O 1s spectrum in Fig. 5(f), the peaks at 530.3, 531.6, and 532.5 eV are assigned to oxygen in Metal–oxygen (M–O), absorbed CO_2 from air and H_2O [68]. After OER, the spectrum of O 1s could be assigned to three peaks, where the peaks at 528.7, 529.9, and 530.9 eV could be attributed to the oxygen in metal–oxygen (M–O), hydroxide (OH^-) and oxygen bound in the absorbed H_2O. According to the above results, after SPD, the elements in printed AlCoCrFeNi HEA exist in the form of a metallic state with partial oxidization. After the process of the OER test, all of the metallic state peaks shift to larger binding energy, which suggests that they are truly active species and contribute to the electrocatalytic activity.

4 Discussion

4.1 Relationship between pore size and SLM process parameters

The preparation of GNP-HEO involves controlling the size of the spinodal decomposition structure during the SLM process. During solidification, the printed AlCoCrFeNi HEA undergoes spinodal decomposition, forming Fe-Cr rich phases and Ni-Al rich phases. These phases have identical structures but differ in composition. The wavelength of the spinodal decomposition correlates directly with the pore size of the nanoporous structure. Previous studies have confirmed that the porous structure is largely determined by the morphology of the precursor alloy [69]. Further insights are derived from Cahn and Charles' research on the kinetic characteristics of spinodal decomposition, which helps in understanding the formation mechanisms of these structures (Eq. (1))

$$\lambda = \sqrt{\frac{8\pi^2 D\theta^2}{\tau T}} \quad (1)$$

where λ is the critical wavelength, T is the spinodal temperature, and θ is below ~ 10% of the spinodal temperature, $D \approx 7.51 \times 10^{-9}$ (m^2/s) is the diffusion coefficient of the AlCoCrFeNi HEA [69], and τ is the cooling rate. The wavelength of the spinodal decomposition component wave curve ranges from 5 to 100 nm. The critical cooling rate required to prevent spinodal decomposition is 3.42×10^{11} m^2/s; cooling rates exceeding this threshold can inhibit the decomposition. In nanoporous high entropy oxides, the critical wavelength of the amplitude-modulated structure is significantly influenced by τ, which is determined by the SLM process parameters, namely P and v. Generally, higher laser power coupled with slower scanning speed results in lower cooling rates, whereas lower laser power and faster scanning speed lead to higher cooling rates. For the spinodal decomposition of AlCoCrFeNi HEA, the factor F is highly sensitive to τ, directly correlating to the heat input represented by P/v during the SLM process. The successful preparation of GNP-HEO relies on precisely tailoring the morphologies of the spinodal decomposition in the precursor alloy through controlled SLM parameters. Understanding the relationship between the porous structure and the cooling rate corresponding to these parameters is crucial. To explore the correlation between cooling rate and wavelength, we utilized the finite element method (FEM) to analyze the effects of P and v on τ during the SLM process, as depicted in Fig. 6. The temperature versus time curves for various laser powers and scanning speeds are shown in Fig. 6(a). A dark-field TEM image, presented in Fig. S9 in the ESM, highlights the nanoscale features of spinodal decomposition and illustrates how the wavelength is directly influenced by the cooling rate. In our simulations, we employed a Gaussian laser heat source model. Here, the cooling rate at $T_{spinodal}$ is selected as the typical τ of laser molten pool solidification, and the

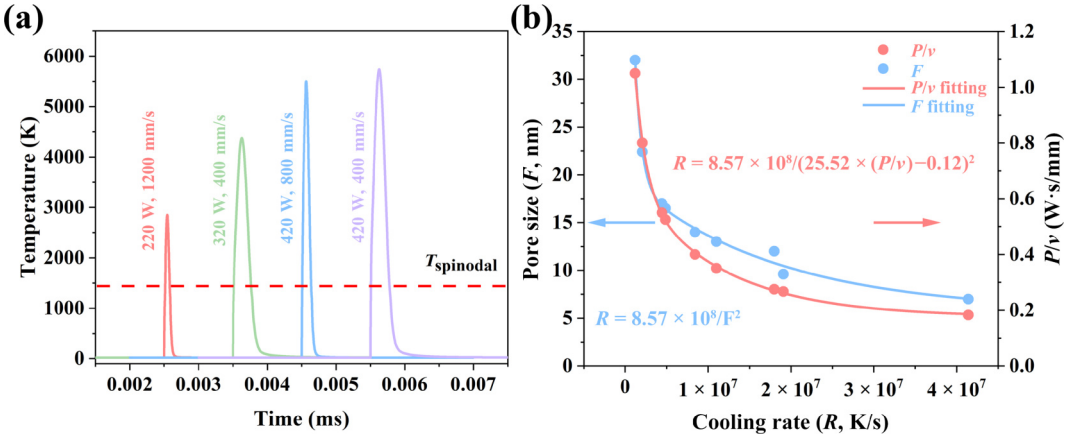

Figure 6 The relationship between pore size and SLM process parameters. (a) Temperature variation curves for several typical laser powers and scanning speeds. (b) The extracted R is a function of P/v and F.

cooling rate of each group of models is calculated when the temperature drops to $T_{spinodal}$ under different process parameters. Figure 6(b) illustrates the extracted τ at $T_{spinodal}$ as a function of P/v and F. It can be seen that P/v increases from 0.183 to 1.050 W·s/mm with the linear energy density, R decreases continuously from 4.12×10^7 to 1.2×10^6 K/s. Meanwhile, F decreases from 32.0 to 7.0 nm with the increase R, as fitted by $R = 8.57 \times 10^8/(25.52 \times (P/v) - 0.12)^2$. The above two equations are combined to $F = -0.12 + 25.52 \times (P/v)$, which agrees with the solid line shown in Fig. 2(a). These findings indicate that as laser power increases and scanning speed decreases, the maximum temperature rises, and consequently, the pore size of the resulting nanoporous high entropy oxide sample after SPD increases. The results underscore that both the spinodal decomposition microstructure and the corresponding pore size are highly sensitive to the cooling rate. In this study, we managed to achieve pore sizes ranging from 7 to 32 nm by adjusting the cooling rate during SLM through changes in process parameters. In summary, these analyses demonstrate that the microstructure of the HEA precursor can be precisely controlled, providing a solid foundation for the preparation of GNP-HEO.

4.2 Accelerating effect of bubble release by gradient nanoporous structure

Previous studies have highlighted that bubbles adhering to the electrode surface during water splitting can isolate reactants from the catalytic site, increasing reaction resistance, consuming more energy, and reducing reaction efficiency. Therefore, understanding the dynamics of bubble release from the electrode surface is critical. GNP-HEO electrodes, thanks to their unique physical structure, facilitate efficient bubble release and exhibit superior OER performance. The efficiency of bubble release is significantly influenced by various forces acting on the bubble, including the buoyancy force (F_b), the surface tension force (F_σ), the hydrodynamic force owing to hydrodynamic pressure (F_h), the contact pressure force (F_{cp}), and electrolysis momentum force (F_{em}) [70, 71]. The balance equation of forces at x-direction as follows (Eq. (2))

$$\sum F_x = F_{\sigma x} + F_{cpx} + F_{hx} + F_{emx} \quad (2)$$

The balance equation of forces at y-direction as follows (Eq. (3))

$$\sum F_y = F_b + F_{\sigma y} + F_{cpy} + F_{hy} + F_{emy} \quad (3)$$

The difficulty of bubble release during water splitting mainly depends on the adhesion force in the y direction. In the ring-shaped pore channel of nanoporous structures, the maximum adhesion force could be estimated as follows

$$F_{\sigma y} = \gamma_{electrolyte}\left(L\pi + D\frac{(4\pi - \pi^2)}{4}\right) \quad (4)$$

where $F_{\sigma y}$ represents the adhesion force in the y-direction when the bubble is released, $\gamma_{electrolyte}$ is the surface tension, D represents the diameter of the ligament, and L denotes the pore size within the electrode. The correlation equation suggests that larger values of L and D increase the adhesion force, which can impede bubble release and increase the overpotential, aligning with the observed OER results. In uniform nanoporous structures, larger pore sizes and ligament diameters contribute to greater resistance to bubble release and higher overpotentials. In contrast, gradient nanoporous structures feature decreasing pore sizes and ligament diameters along the bubble release direction, promoting the division of larger bubbles into smaller ones. This reduction in bubble size during release decreases the force on the bubbles, ensuring adequate exposure of active sites and facilitating efficient catalysis. In addition, due to the unique gradient nanoporous structure, there is a large pressure difference between the two parts, which is beneficial to accelerate the expulsion of bubbles and reduce the increase of additional overpotential due to the plugging and aggregation of bubbles, the schematic diagram is shown in Fig. 7. Therefore, the gradient nanoporous structure can promote the rapid release of bubbles and improve the OER activity of the electrode.

4.3 Theoretical calculation of OER

To elucidate the catalytic mechanism of NP-HEO during the OER, DFT was employed to identify the active catalytic origins. The oxygen evolution process typically follows two electron-transfer routes: the adsorbate evolution mechanism (AEM) and the lattice oxygen oxidation mechanism (LOM) [72]. Figure S10 in the ESM illustrates the adsorption configurations of reaction intermediates on nanoporous AlCoCrFeNi oxides for both the AEM and LOM mechanisms. Figure 8 presents the Gibbs free energy diagrams for OER on NP-HEO under AEM and LOM. These diagrams show that at potentials of 0 and 1.23 V, the presence of oxygen vacancies strengthens the adsorption between the catalyst and the intermediates. In the AEM pathway, the metal site acts as the active

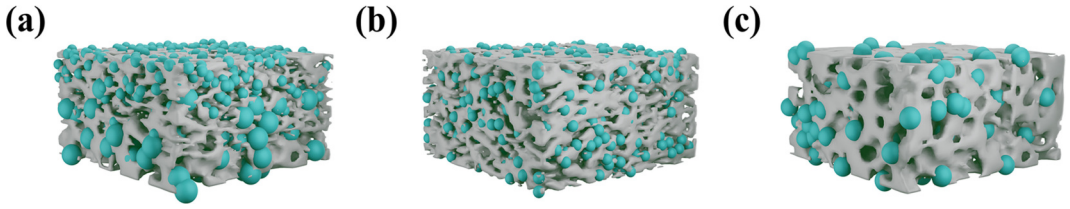

Figure 7 Schematic diagram of bubble release behavior in different structures. (a)–(c) Bubble release process in GNP-HEO, uniform small pores (pore size = 7 nm), and uniform large pores (pore size = 32 nm).

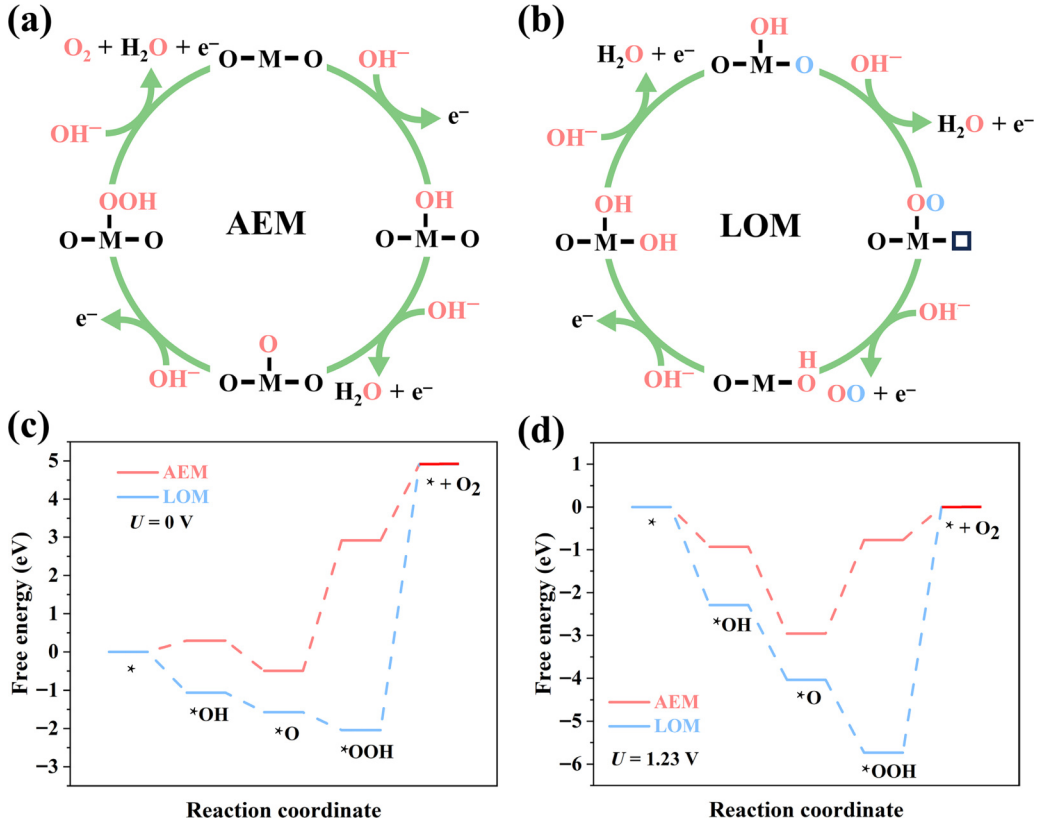

Figure 8 Theoretical calculation of OER on AlCoCrFeNi high-entropy oxides. (a) and (b) Schematic illustrations of the AEM and LOM pathways on the NP-HEO. (c) and (d) The free energy diagram of OER on the NP-HEO at $U = 0$ V and $U = 1.23$ V.

center, with the conversion of *O to *OH identified as the potential-determining step (PDS), featuring an energy barrier of 3.41 eV. Conversely, in the LOM pathway, the conversion of *OOH to * + O_2 is the PDS, with a significantly higher energy barrier of 6.96 eV. The lower the energy barrier of the PDS, the more favorable the reaction and the better the catalytic activity, indicating that the AEM mechanism is more advantageous for NP-HEO.

5 Conclusions

In summary, we fabricated a wood stem-like NP-HEO electrode with a controllable pore size. The objective is to accelerate the de of bubbles from water decomposition in gradient nanoporous high-entropy oxides, thereby reducing energy loss—a crucial factor for high-performance electrocatalysts. Our research findings demonstrate that the pore size in nanoporous high entropy oxides is intricately linked to the microstructure of the precursor alloys, which in turn is significantly influenced by the cooling rate. By adjusting the printing parameters, precise control over the nanoporous structure is achieved. Additionally, the GNP-HEO electrode showcased exceptional OER performance in alkaline electrolytes, exhibiting an overpotential of just 250 mV at 50 mA/cm^2 and a Tafel slope of 38 mV/dec. The superior OER properties are attributed to the rapid bubble release and enhanced exposure of active sites. Our work provides a new option for the simple preparation of efficient and stable OER electrocatalysts.

Electronic Supplementary Material: Supplementary material (XRD patterns, SEM images, TEM images, and theoretical models) is available in the online version of this article at https://doi.org/10.26599/NR.2025.94907002.

Data availability

All data needed to support the conclusions in the paper are presented in the manuscript and the Electronic Supplementary Material. Additional data related to this paper may be requested from the corresponding author upon request.

Acknowledgements

This work is supported by the Guangdong Province SpecialFunding

Project for the Development of Marine Economy (No. GDNRC[2024]41), the National Key Research and DevelopmentProgram of China (No. 2023YFB3408101), and the Dalian YouthScience and Technology Star Project (No. 2021RQ103).

Declaration of competing interest

All the contributing authors report no conflict of interests in this work.

Author contribution statement

W. W.: Conceptualization, data curation, investigation, methodology, validation, writing – original draft. W. Q. W.: Investigation, writing – original draft, data curation, experimental design. H. H. W.: Writing – review & editing, funding acquisition. X. L.: Writing – review & editing, project administration, resources. J. W. Z.: Writing – review & editing, funding acquisition. Y. Z. L.: Writing – original draft, writing – review & editing, project administration, funding acquisition, resources, supervision. All the authors have approved the final manuscript.

Use of AI statement

None.

References

[1] Zhang, Y. Z.; Zhu, Z. Z.; Guo, X.; Qi, J. Y.; Li, X. Plasma-assisted seconds-level-impregnated preparation of bifunctional N-doped NiCoP with O vacancies enhancement: Driving efficient water splitting. *Chem. Eng. J.* **2023**, *452*, 139230.

[2] Li, S. J.; Xie, W. F.; Song, Y. K.; Li, Y.; Song, Y. J.; Li, J. Z.; Shao, M. F. Integrated CoPt electrocatalyst combined with upgrading anodic reaction to boost hydrogen evolution reaction. *Chem. Eng. J.* **2022**, *437*, 135473.

[3] Wang, K. X.; Zhao, R. C.; Wang, Z. J.; Zhang, X. X.; Ouyang, A. X.; Zhou, C. J.; Zhou, W.; Tan, X. Y.; Chu, Y. Y. Controlled tuning the morphology of CoNiP catalysts with ultra-high activity for water splitting at large current densities in alkaline medium. *Appl. Surf. Sci.* **2023**, *626*, 157218.

[4] Cao, L. L.; Luo, Q. Q.; Chen, J. J.; Wang, L.; Lin, Y.; Wang, H. J.; Liu, X. K.; Shen, X. Y.; Zhang, W.; Liu, W. et al. Dynamic oxygen adsorption on single-atomic ruthenium catalyst with high performance for acidic oxygen evolution reaction. *Nat. Commun.* **2019**, *10*, 4849.

[5] Zhu, J.; Du, Q. X.; Khan, M. A.; Zhao, H. B.; Fang, J. H.; Ye, D. X.; Zhang, J. J. 2D porous Co-Mo nitride heterostructures nanosheets for highly effective electrochemical water splitting. *Appl. Surf. Sci.* **2023**, *623*, 156989.

[6] Odella, E.; Mora, S. J.; Wadsworth, B. L.; Goings, J. J.; Gervaldo, M. A.; Sereno, L. E.; Groy, T. L.; Gust, D.; Moore, T. A.; Moore, G. F. et al. Proton-coupled electron transfer across benzimidazole bridges in bioinspired proton wires. *Chem. Sci.* **2020**, *11*, 3820–3828.

[7] Hao, J. C.; Zhuang, Z. C.; Cao, K. C.; Gao, G. H.; Wang, C.; Lai, F. L.; Lu, S. L.; Ma, P. M.; Dong, W. F.; Liu, T. X. et al. Unraveling the electronegativity-dominated intermediate adsorption on high-entropy alloy electrocatalysts. *Nat. Commun.* **2022**, *13*, 2662.

[8] Zhou, Z. Y.; Liang, R. K.; Weng, S.; Lei, F. J.; Qian, Y. L.; Yang, Z.; Yang, H. Y.; Chen, Z. L.; Hao, W. J. Construction of filterable and intelligent flexible NiB-based catalytic electrode toward efficient overall seawater splitting. *Appl. Surf. Sci.* **2023**, *640*, 158415.

[9] Zerdoumi, R.; Savan, A.; Amalraj, M.; Tetteh, E. B.; Lourens, F.; Krysiak, O. A.; Junqueira, J. R. C.; Ludwig, A.; Schuhmann, W. Combinatorial screening of electronic and geometric effects in compositionally complex solid solutions toward a rational design of electrocatalysts. *Adv. Energy Mater.* **2024**, *14*, 2302177.

[10] Han, Y. J.; Tian, M.; Wang, C. J.; Zong, T.; Wang, X. D. High-entropy spinel oxide $(Fe_{0.2}Mg_{0.2}Mn_{0.1}Al_{0.3}Cr_{0.2})_3O_4$ as a highly active and stable redox material for methane driven solar thermochemical water splitting. *Appl. Catal. B: Environ.* **2023**, *339*, 123096.

[11] Zhang, Q. W.; Hu, Y. X.; Wu, H. F.; Zhao, X. R.; Wang, M. L.; Wang, S. H.; Feng, R. H.; Chen, Q.; Song, F.; Chen, M. W. et al. Entropy-stabilized multicomponent porous spinel nanowires of $NiFeXO_4$ (X = Fe, Ni, Al, Mo, Co, Cr) for efficient and durable electrocatalytic oxygen evolution reaction in alkaline medium. *ACS Nano* **2023**, *17*, 1485–1494.

[12] Li, R.; Liu, X. J.; Liu, W. H.; Li, Z. B.; Chan, K. C.; Lu, Z. P. Design of hierarchical porosity via manipulating chemical and microstructural complexities in high‐entropy alloys for efficient water electrolysis. *Adv. Sci.* **2022**, *9*, 2105808.

[13] Iwata, R.; Zhang, L. N.; Wilke, K. L.; Gong, S.; He, M. F.; Gallant, B. M.; Wang, E. N. Bubble growth and departure modes on wettable/non-wettable porous foams in alkaline water splitting. *Joule* **2021**, *5*, 887–900.

[14] Yin, W. N.; Yuan, L. X.; Huang, H.; Cai, Y. T.; Pan, J. A.; Sun, N.; Zhang, Q. Y.; Shu, Q. H.; Gu, C.; Zhuang, Z. C. et al. Strategies to accelerate bubble detachment for efficient hydrogen evolution. *Chin. Chem. Lett.* **2023**, *35*, 108351.

[15] Dastafkan, K.; Meyer, Q.; Chen, X. J.; Zhao, C. Efficient oxygen evolution and gas bubble release achieved by a low gas bubble adhesive iron-nickel vanadate electrocatalyst. *Small* **2020**, *16*, 2002412.

[16] Kaya, M. F.; Demir, N.; Rees, N. V.; El-Kharouf, A. Magnetically modified electrocatalysts for oxygen evolution reaction in proton exchange membrane (PEM) water electrolyzers. *Int. J. Hydrogen Energy* **2021**, *46*, 20825–20834.

[17] Liu, Z. Q.; Meyers, M. A.; Zhang, Z. F.; Ritchie, R. O. Functional gradients and heterogeneities in biological materials: Design principles, functions, and bioinspired applications. *Prog. Mater. Sci.* **2017**, *88*, 467–498.

[18] Pauly, S.; Wang, P.; Kühn, U.; Kosiba, K. Experimental determination of cooling rates in selectively laser-melted eutectic Al-33Cu. *Addit. Manuf.* **2018**, *22*, 753–757.

[19] Wang, X.; Zhang, C. H.; Cui, X.; Zhang, S.; Chen, J.; Zhang, J. B. Novel gradient alloy steel with quasi-continuous ratios fabricated by SLM: Material microstructure and wear mechanism. *Mater. Charact.* **2021**, *174*, 111020.

[20] Gu, Z. X.; Zhang, Y. C.; Wei, X. L.; Duan, Z. Y.; Ren, L.; Ji, J. C.; Zhang, X. Q.; Zhang, Y. X.; Gong, Q. Y.; Wu, H. et al. Unveiling the accelerated water electrolysis kinetics of heterostructural iron-cobalt-nickel sulfides by probing into crystalline/amorphous interfaces in stepwise catalytic reactions. *Adv. Sci.* **2022**, *9*, 2201903.

[21] Yu, X.; Pan, Z. Q.; Zhao, Z. X.; Zhou, Y. K.; Pei, C. G.; Ma, Y. F.; Park, H. S.; Wang, M. Boosting the oxygen evolution reaction by controllably constructing $FeNi_3$/C nanorods. *Nanomaterials* **2022**, *12*, 2525.

[22] Li, D. J.; Li, Q. H.; Gu, Z. G.; Zhang, J. A surface-mounted MOF thin film with oriented nanosheet arrays for enhancing the oxygen evolution reaction. *J. Mater. Chem. A* **2019**, *7*, 18519–18528.

[23] He, Q.; Hu, H. H.; Shao, Y. B.; Tang, D.; Zhao, Z. Z. Constructing 3D hierarchical MOFs nanospheres for oxygen evolution from high-throughput calculations. *J. Colloid Interface Sci.* **2022**, *607*, 1944–1952.

[24] Liu, Z. S.; Xu, J. L.; Zhang, F.; Ji, L.; Shi, Z. N. Defect-rich high-entropy oxide nanospheres anchored on high-entropy MOF nanosheets for oxygen evolution reaction. *Int. J. Hydrogen Energy* **2023**, *48*, 14622–14632.

[25] Chen, C.; Tuo, Y. X.; Lu, Q.; Lu, H.; Zhang, S. Y.; Zhou, Y.; Zhang,

J.; Liu, Z. N.; Kang, Z. X.; Feng, X. et al. Hierarchical trimetallic Co-Ni-Fe oxides derived from core–shell structured metal-organic frameworks for highly efficient oxygen evolution reaction. *Appl. Catal. B: Environ.* **2021**, *287*, 119953.

[26] Wang, H.; Gu, M. Z.; Huang, X. M.; Gao, A.; Liu, X. D.; Sun, P.; Zhang, X. J. Ligand-based modulation of the electronic structure at metal nodes in MOFs to promote the oxygen evolution reaction. *J. Mater. Chem. A* **2023**, *11*, 7239–7245.

[27] Zheng, X. Y.; Jia, G.; Fan, G. Z.; Luo, W. J.; Li, Z. S.; Zou, Z. G. Modulation of disordered coordination degree based on surface defective metal-organic framework derivatives toward boosting oxygen evolution electrocatalysis. *Small* **2020**, *16*, 2003630.

[28] Wei, X. D.; Li, N.; Liu, N. Ultrathin NiFeZn–MOF nanosheets containing few metal oxide nanoparticles grown on nickel foam for efficient oxygen evolution reaction of electrocatalytic water splitting. *Electrochim. Acta* **2019**, *318*, 957–965.

[29] Wei, H. H.; Li, J.; Du, P.; Zhang, L. T.; Su, Z. X.; Li, H.; Lei, M.; Gong, X. Q.; Huang, K. Electronic optimization and modification of efficient Ir clusters embedded onto Ni-Mo-P for electrocatalytic oxygen evolution reaction. *Adv. Compos. Hybrid Mater.* **2023**, *6*, 37.

[30] Gu, Y. H.; Wang, X. Y.; Bao, A.; Dong, L.; Zhang, X. Y.; Pan, H. J.; Cui, W. Q.; Qi, X. W. Enhancing electrical conductivity of single-atom doped Co_3O_4 nanosheet arrays at grain boundary by phosphor doping strategy for efficient water splitting. *Nano Res.* **2022**, *15*, 9511–9519.

[31] Liu, H. B.; Jia, Q. H.; Huang, S. Q.; Yang, L.; Wang, S. T.; Zheng, L. R.; Cao, D. P. Ultra-small Ru nanoparticles embedded on Fe-Ni$(OH)_2$ nanosheets for efficient water splitting at a large current density with long-term stability of 680 hours. *J. Mater. Chem. A* **2022**, *10*, 4817–4824.

[32] Wang, X.; Zhao, P. D.; Ling, L.; Luo, Y. C.; Li, Z.; Jiao, Z.; Cheng, L. L. Optimizing the electronic structure of $NiSe_2$/$CoSe_2$ nanosheet arrays by phosphorus doping for high-efficiency oxygen evolution electrocatalysts. *J. Alloys Compd.* **2022**, *927*, 166845.

[33] Zheng, X. Z.; Sun, A. W.; Qiu, Y. L.; Wang, Z. X.; Xu, J. T.; Liu, J. Q. Controllable atoms implantation for inducing high valency nickel towards optimizing electronic structure for enhanced overall water splitting. *J. Colloid Interface Sci.* **2023**, *650*, 1966–1973.

[34] Yuan, M. L.; Wang, M.; Lu, P. L.; Sun, Y.; Dipazir, S.; Zhang, J. X.; Li, S. W.; Zhang, G. J. Tuning carbon nanotube-grafted core–shell-structured cobalt selenide@carbon hybrids for efficient oxygen evolution reaction. *J. Colloid Interface Sci.* **2019**, *533*, 503–512.

[35] Cao, X.; Medvedeva, J. E.; Nath, M. Copper cobalt selenide as a high-efficiency bifunctional electrocatalyst for overall water splitting: Combined experimental and theoretical study. *ACS Appl. Energy Mater.* **2020**, *3*, 3092–3103.

[36] Du, X. Q.; Ding, Y. Y.; Zhang, X. S. Selectively Se-doped Co_3O_4@CeO_2 nanoparticle-dotted nanoneedle arrays for high-efficiency overall water splitting. *Appl. Surf. Sci.* **2021**, *562*, 150227.

[37] Yang, H. Y.; Dai, G. L.; Chen, Z. L.; Wu, J.; Huang, H.; Liu, Y.; Shao, M. W.; Kang, Z. H. Pseudo-periodically coupling Ni–O lattice with Ce–O lattice in ultrathin heteronanowire arrays for efficient water oxidation. *Small* **2021**, *17*, 2101727.

[38] Zheng, L. X.; Zhao, Y. J.; Bao, Z. Y.; Xu, P. H.; Jia, Y.; Wang, Y. Z.; Yang, P. J.; Shi, X. W.; Wu, Q.; Zheng, H. J. High-valence Mo doping and oxygen vacancy engineering to promote morphological evolution and oxygen evolution reaction activity. *ACS Appl. Mater. Interfaces* **2023**, *15*, 43953–43962.

[39] Xue, H. Y.; Meng, A. L.; Yang, T. Q.; Li, Z. J.; Chen, C. J. Controllable oxygen vacancies and morphology engineering: Ultra-high HER/OER activity under base-acid conditions and outstanding antibacterial properties. *J. Energy Chem.* **2022**, *71*, 639–651.

[40] Wang, H. B.; Du, X. Q.; Zhang, X. S.; Li, L. Controlled synthesis of M doped Co_3O_4 (M = Ce, Ni and Fe) on Ni foam as robust electrocatalyst for oxygen evolution reaction and urea oxidation reaction. *J. Colloid Interface Sci.* **2023**, *630*, 512–524.

[41] Fan, C.; Wu, X. D.; Li, M.; Wang, X.; Zhu, Y.; Fu, G. T.; Ma, T. Y.; Tang, Y. W. Surface chemical reconstruction of hierarchical hollow inverse-spinel manganese cobalt oxide boosting oxygen evolution reaction. *Chem. Eng. J.* **2022**, *431*, 133829.

[42] Wen, M. J.; Li, Z. H.; Wang, R.; Li, Z. M.; Liu, X.; Wang, G. X.; Xie, G. W.; Jiang, L. H. Facile electrodeposited amorphous Co-Mo-Fe electrocatalysts for oxygen evolution reaction. *Int. J. Hydrogen Energy* **2022**, *47*, 12506–12514.

[43] Tang, D.; Ma, Y. F.; Liu, Y.; Wang, K. K.; Liu, Z.; Li, W. Z.; Li, J. Amorphous three-dimensional porous Co_3O_4 nanowire network toward superior OER catalysis by lithium-induced. *J. Alloys Compd.* **2022**, *893*, 162287.

[44] Sun, Z. M.; Lin, L.; Nan, C. Y.; Li, H. F.; Sun, G. B.; Yang, X. J. Amorphous boron oxide coated NiCo layered double hydroxide nanoarrays for highly efficient oxygen evolution reaction. *ACS Sustain. Chem. Eng.* **2018**, *6*, 14257–14263.

[45] Jiao, T.; Lian, Q.; Zhao, T. Z.; Wang, H. C. Influence of ink properties and voltage parameters on piezoelectric inkjet droplet formation. *Appl. Phys. A* **2021**, *127*, 11.

[46] Zhu, Y. X.; Jiang, M. Y.; Liu, M.; Wu, L. K.; Hou, G. Y.; Tang, Y. P. An Fe–V@NiO heterostructure electrocatalyst towards the oxygen evolution reaction. *Nanoscale* **2020**, *12*, 3803–3811.

[47] Huang, S. S.; Zhang, Q.; Xin, P. J.; Zhang, J.; Chen, Q. C.; Fu, J.; Jin, Z. Q.; Wang, Q.; Hu, Z. J. Construction of Fe‐doped NiS–NiS_2 heterostructured microspheres via etching Prussian blue analogues for efficient water-urea splitting. *Small* **2022**, *18*, 2106841.

[48] Gautam, J.; Chanda, D.; Meshesha, M. M.; Jang, S. G.; Yang, B. L. Manganese cobalt sulfide/molybdenum disulfide nanowire heterojunction as an excellent bifunctional catalyst for electrochemical water splitting. *J. Colloid Interface Sci.* **2023**, *638*, 658–671.

[49] Zhang, Y. Y.; Chen, M. X.; Guo, P.; Du, Y. C.; Song, B.; Wang, X. J.; Jiang, Z. X.; Xu, P. Magnetic field-enhanced water splitting enabled by bifunctional molybdenum-doped nickel sulfide on nickel foam. *Carbon Energy* **2023**, *5*, e351.

[50] Wang, J. Z.; Luo, Y.; Wang, J. W.; Yu, H. L.; Guo, Z. Y.; Yang, J.; Xue, Y. N.; Cai, N.; Li, H.; Yu, F. Q. One-pot self-assembled bimetallic sulfide particle cluster-supported three-dimensional graphene aerogel as an efficient electrocatalyst for the oxygen evolution reaction. *Phys. Chem. Chem. Phys.* **2023**, *25*, 26298–26307.

[51] Li, K. X.; Feng, D. M.; Tong, Y. Hierarchical metal sulfides heterostructure as superior bifunctional electrode for overall water splitting. *ChemSusChem* **2022**, *15*, e202200590.

[52] Zhang, R. L.; Duan, J. J.; Feng, J. J.; Mei, L. P.; Zhang, Q. L.; Wang, A. J. Walnut kernel-like iron-cobalt-nickel sulfide nanosheets directly grown on nickel foam: A binder-free electrocatalyst for high-efficiency oxygen evolution reaction. *J. Colloid Interface Sci.* **2021**, *587*, 141–149.

[53] Liu, H. B.; Gao, J.; Xu, X. C.; Jia, Q. H.; Yang, L.; Wang, S. T.; Cao, D. P. Oriented construction Cu_3P and Ni_2P heterojunction to boost overall water splitting. *Chem. Eng. J.* **2022**, *448*, 137706.

[54] Xiao, M.; Zhang, C.; Wang, P.; Zeng, W.; Zhu, J.; Li, Y.; Peng, W.; Liu, Q.; Xu, H.; Zhao, Y. et al. Polymetallic phosphides evolved from MOF and LDH dual-precursors for robust oxygen evolution reaction in alkaline and seawater media. *Mater. Today Phys.* **2022**, *24*, 100684.

[55] Xiao, Y. P.; Chen, X.; Li, T. L.; Mao, Y. Y.; Liu, C. L.; Chen, Y. C.; Wang, W. J. Mo-doped cobalt hydroxide nanosheets coupled with cobalt phosphide nanoarrays as bifunctional catalyst for efficient and high-stability overall water splitting. *Int. J. Hydrogen Energy* **2022**, *47*, 9915–9924.

[56] Yang, Z. J.; Tuo, Y. X.; Lu, Q.; Chen, C.; Liu, M. S.; Liu, B. Y.; Duan, X. Z.; Zhou, Y.; Zhang, J. Hierarchical Cu_3P-based nanoarrays on nickel foam as efficient electrocatalysts for overall water splitting. *Green Energy Environ.* **2022**, *7*, 236–245.

[57] Xie, H. P.; Lan, C.; Chen, B.; Wang, F. H.; Liu, T. Noble-metal-free

catalyst with enhanced hydrogen evolution reaction activity based on granulated Co-doped Ni-Mo phosphide nanorod arrays. *Nano Res.* **2020**, *13*, 3321–3329.

[58] Ye, F.; Ma, X. F.; Cao, Y. P.; Yang, Y. K.; Zhang, T. Y.; Wang, K. C.; Feng, Y. C.; La, T.; Xu, C. Heterogeneous layered multiple transition metal composite electrocatalysts with controlled composition for hydrogen production. *Int. J. Hydrogen Energy* **2023**, *48*, 1733–1746.

[59] Zhang, J. J.; Li, M. Y.; Bao, W. W.; Feng, X. H.; Liu, G.; Yang, C. M.; Guo, N.; Zhang, N. N. Cr-doped NiZn layered double hydroxides with surface reconstruction toward the enhanced water splitting. *Colloids Surf. A: Physicochem. Eng. Aspects* **2022**, *649*, 129324.

[60] Zheng, Z. C.; Guo, Y. R.; Wan, H.; Chen, G.; Zhang, N.; Ma, W.; Liu, X. H.; Liang, S. Q.; Ma, R. Z. Anchoring active sites by Pt_2FeNi alloy nanoparticles on NiFe layered double hydroxides for efficient electrocatalytic oxygen evolution reaction. *Energy Environ. Mater.* **2022**, *5*, 270–277.

[61] Zhou, Y. N.; Yu, W. L.; Cao, Y. N.; Zhao, J.; Dong, B.; Ma, Y.; Wang, F. L.; Fan, R. Y.; Zhou, Y. L.; Chai, Y. M. S-doped nickel-iron hydroxides synthesized by room-temperature electrochemical activation for efficient oxygen evolution. *Appl. Catal. B: Environ. Energy* **2021**, *292*, 120150.

[62] Li, Z. Y.; Zhang, Y.; Liu, Z. S.; Sun, H. B.; Shi, Z. N.; Xu, J. L. Enhanced electrocatalytic performance of NiFe layered double hydroxide for oxygen evolution reaction by CoW surface codoping. *Int. J. Hydrogen Energy* **2024**, *51*, 895–903.

[63] Ding, C. F.; Liu, T. Y.; Yan, X. D.; Huang, L. B.; Ryu, S.; Lan, J. L.; Yu, Y. H.; Zhong, W. H.; Yang, X. P. An ultra-microporous carbon material boosting integrated capacitance for cellulose-based supercapacitors. *Nano-Micro Lett.* **2020**, *12*, 63.

[64] Jiao, W.; Liu, P.; Lin, H. J.; Zhou, W.; Wang, Z.; Fujita, T.; Hirata, A.; Li, H. W.; Chen, M. W. Tunable nanoporous metallic glasses fabricated by selective phase dissolution and passivation for ultrafast hydrogen uptake. *Chem. Mater.* **2017**, *29*, 4478–4483.

[65] Wu, L. H.; Li, Q.; Wu, C. H.; Zhu, H. Y.; Mendoza-Garcia, A.; Shen, B.; Guo, J. H.; Sun, S. H. Stable cobalt nanoparticles and their monolayer array as an efficient electrocatalyst for oxygen evolution reaction. *J. Am. Chem. Soc.* **2015**, *137*, 7071–7074.

[66] Anantharaj, S.; Venkatesh, M.; Salunke, A. S.; Simha, T. V. S. V.; Prabu, V.; Kundu, S. High-performance oxygen evolution anode from stainless steel via controlled surface oxidation and Cr removal. *ACS Sustain. Chem. Eng.* **2017**, *5*, 10072–10083.

[67] Tang, J.; Xu, J. L.; Ye, Z. G.; Li, X. B.; Luo, J. M. Microwave sintered porous CoCrFeNiMo high entropy alloy as an efficient electrocatalyst for alkaline oxygen evolution reaction. *J. Mater. Sci. Technol.* **2021**, *79*, 171–177.

[68] Gao, G. J.; Xu, J. L.; Tang, J.; Zhang, L. W.; Ma, Y. C.; Luo, J. M. Plasma nitrided CoCrFeNiMn high entropy alloy coating as a self-supporting electrode for oxygen evolution reaction. *J. Mater. Res. Technol.* **2023**, *23*, 5357–5367.

[69] Li, W. X.; Luo, B.; Huang, H. T.; Liu, Y.; Wang, W.; Luo, J. R.; Fu, B. Q. A comparative study of deuterium permeation behaviors of CoCrMnFeNi and AlCoCrFeNi high entropy alloys. *Int. J. Hydrogen Energy* **2023**, *48*, 19657–19665.

[70] Taqieddin, A.; Nazari, R.; Rajic, L.; Alshawabkeh, A. Review-physicochemical hydrodynamics of gas bubbles in two phase electrochemical systems. *J. Electrochem. Soc.* **2017**, *164*, E448–E459.

[71] Hong, G.; Yan, X.; Yang, Y. H.; Xie, T. Z.; Xu, J. J. Bubble departure size in forced convective subcooled boiling flow under static and heaving conditions. *Nucl. Eng. Des.* **2012**, *247*, 202–211.

[72] Lu, M.; Zheng, Y.; Hu, Y.; Huang, B. L.; Ji, D. G.; Sun, M. Z.; Li, J. Y.; Peng, Y.; Si, R.; Xi, P. X. et al. Artificially steering electrocatalytic oxygen evolution reaction mechanism by regulating oxygen defect contents in perovskites. *Sci Adv.* **2022**, *8*, eabq3563.